nature physics

Article

https://doi.org/10.1038/s41567-023-01975-y

Observation of temporal reflection and broadband frequency translation at photonic time interfaces

Received: 11 November 2022

Accepted: 1 February 2023

Published online: 13 March 2023

Check for updates

Hady Moussa[1,2,5], Gengyu Xu[1,5], Shixiong Yin[1,2,5], Emanuele Galiffi[1], Younes Ra'di[1,3] & Andrea Alù[1,2,4]

Time reflection is a uniform inversion of the temporal evolution of a signal, which arises when an abrupt change in the properties of the host material occurs uniformly in space. At such a time interface, a portion of the input signal is time reversed, and its frequency spectrum is homogeneously translated as its momentum is conserved, forming the temporal counterpart of a spatial interface. Combinations of time interfaces, forming time metamaterials and Floquet matter, exploit the interference of multiple time reflections for extreme wave manipulation, leveraging time as an additional degree of freedom. Here we report the observation of photonic time reflection and associated broadband frequency translation in a switched transmission-line metamaterial whose effective capacitance is homogeneously and abruptly changed via a synchronized array of switches. A pair of temporal interfaces are combined to demonstrate time-reflection-induced wave interference, realizing the temporal counterpart of a Fabry–Pérot cavity. Our results establish the foundational building blocks to realize time metamaterials and Floquet photonic crystals, with opportunities for extreme photon manipulation in space and time.

Reflection is a universal phenomenon occurring when a travelling wave encounters an inhomogeneity. Spatial reflections arise at a sharp discontinuity in space: here momentum is exchanged between an incoming wave and the interface, which acts as a momentum bath, as frequency is conserved. As the basis of wave scattering, spatial reflections play a key role in wave control and routing, as well as in the formation of resonant modes, filtering, band engineering and metamaterial responses. Recently, advances across nonlinear wave sciences have stirred substantial interest in the use of time as an additional degree of freedom for wave scattering, leveraging time-varying media as reservoirs that mix and exchange energy with waves in the system. As examples of these opportunities, photonic time crystals and Floquet wave phenomena have raised interest across the broader physics community[1–8]. In this context, time reflection (TR) constitutes the temporal counterpart of spatial reflection, with dual features. This effect occurs at a time interface, that is, when the properties of the host medium are homogeneously switched in space over a timespan much faster than the wave dynamics. On TR, an input wave is partly time reversed: its energy and frequency content are generally transformed as momentum is conserved because of spatial translational symmetry[9,10].

Time reversal is a key functionality for a variety of applications, from channel estimation in communication systems to compensation of signal distortion and dispersion. The most common way of realizing time reversal is through the digitization and retransmission of a recorded signal through a computer[11], but with notable

[1]Photonics Initiative, Advanced Science Research Center, City University of New York, New York, NY, USA. [2]Department of Electric Engineering, City College of City University of New York, New York, NY, USA. [3]Department of Electrical Engineering and Computer Science, Syracuse University, Syracuse, NY, USA. [4]Physics Program, Graduate Center, City University of New York, New York, NY, USA. [5]These authors contributed equally: Hady Moussa, Gengyu Xu, Shixiong Yin. e-mail: aalu@gc.cuny.edu

https://doi.org/10.1038/s41567-023-01975-y

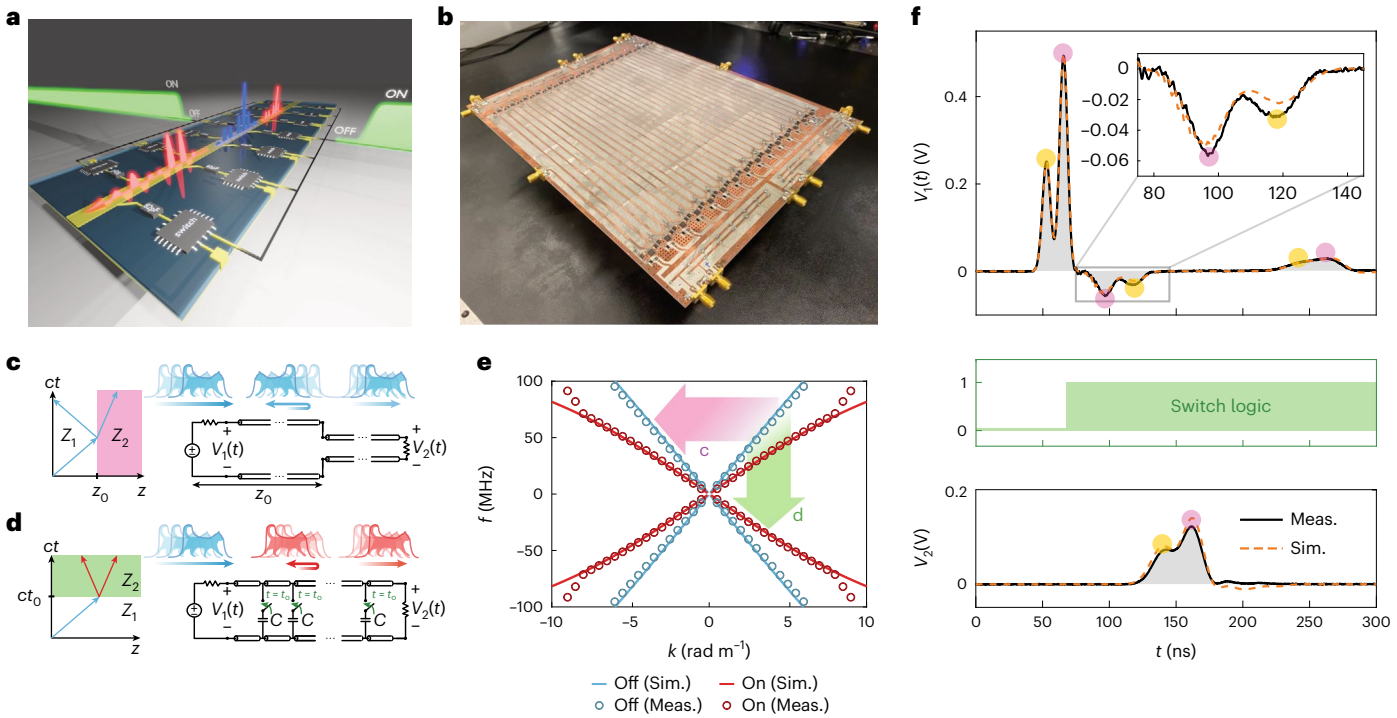

Fig. 1 | Observation of photonic TR. a, Illustration of a time interface in a uniformly switched TLM. A step-like bias signal (green) is used to uniformly activate a set of switches distributed along the TLM, with spacing much smaller than the wavelengths of operation. On closing (opening) of the switches, the effective TLM impedance is abruptly decreased (increased) by a factor of two, causing a broadband forward-propagating signal (blue) to be split into a time-refracted and TR signal, both with redshifted frequencies (red). **b**, Photograph of the fabricated time-switched TLM. **c**, Reflection at a spatial interface causes the reflected signal to invert its profile in space. **d**, A temporal interface breaks time-translation symmetry in a spatially homogeneous medium, uniformly inverting the evolution of an input signal in time. **e**, Simulated (Sim.) and measured (Meas.) dispersion relations of the fabricated TLM before (blue) and after (red) activating the switches. The purple arrow indicates broadband transitions induced by spatial reflection, coupling positive and negative momenta, whereas the green arrow indicates TR, coupling positive and negative frequencies. **f**, Experimental observation of photonic TR at a time interface with an asymmetric pulse consisting of a smaller input signal (yellow marker in input port voltage V_1) followed by a larger one (purple marker). Within 3 ns after the switch logic (middle) turns on, a portion of the input signal undergoes TR, propagating back to the input port, where the two signals are measured in reverse order (purple marker and then yellow marker; zoomed-in view in the inset), with flipped polarity. After ~140 ns, the time-refracted signal, having undergone a spatial reflection at the end of the TLM, returns to the V_1 port in the original yellow–purple order. The output port voltage V_2 shows the time-refracted signal (bottom), broadened in time due to the broadband redshift in its frequency content induced by the time interface. Signal amplitudes are plotted accounting for the power lost in the splitter and impedance change (Supplementary Section 3).

requirements in terms of processing time and energy, as well as memory demands. In the analogue domain, time reversal can be achieved by periodically modulating the properties of the host medium at twice the frequency of the signal. This phenomenon has been observed in acoustics[12] and magnonics[13], as well as for electromagnetic waves at both radio-frequencies[11] and with lower efficiency in optics[14]. However, parametric phenomena are inherently slow and narrowband, relying on extended exposure of the signal of interest to a periodic modulation driving the resonant coupling between the positive and negative frequencies[14] and hence subject to instabilities leading to highly dispersive and nonlinear distortions. On the contrary, TR at a time interface enables ultrafast and ultrabroadband time reversal and—where desirable—efficient frequency translation of an arbitrary waveform. Although several exciting theoretical proposals have been put forward to exploit these features for a variety of exotic photonic functionalities, including subwavelength focusing[15] imaging through random media[16], temporal anti-reflection coatings and advanced frequency filtering[17], inverse prisms[18], temporal aiming[19], analogue computing[20] and the ultrafast generation of squeezed states of quantum light[21], time interfaces have so far been observed only for water waves[22], remaining elusive to photonics and thus drastically limiting their impact. The key challenge in this quest consists of designing and realizing a setup capable of imparting sufficiently strong and fast variations to the electromagnetic properties of a material uniformly in space and hence requiring a metamaterial featuring a temporal response much faster than temporal wave dynamics. Energy and dispersion requirements may also become very demanding when imparting such strong and fast modulations of the material properties[23], factors that have been hindering the experimental demonstration of TR in electromagnetics to date.

Here we are able to tackle these challenges, and demonstrate time interfaces and TR in a microwave transmission-line metamaterial (TLM) periodically loaded by a deeply subwavelength array of lumped capacitors, synchronously added to, or removed from, a microstrip through voltage-controlled reflective switches. On switching, we can uniformly and strongly change the effective capacitance per unit length of the TLM much faster than the temporal variations of the broadband signals propagating through it. This realizes a time interface, with associated photonic TR, as well as broadband, efficient frequency translation (Fig. 1a). As we discuss in the following, by switching the capacitive loads in and out, we are able to drastically and abruptly modify the electromagnetic properties of the TLM without affecting its linear dispersion and without large energy requirements. By implementing a pair of such time interfaces, we form a temporal slab in which the reflected and refracted signals at each time interface interfere, demonstrating the temporal analogue of a Fabry–Pérot filter[17]. Our results establish the

fundamental building blocks to exploit time as an additional degree of freedom for extreme wave manipulation in metamaterials[24–26].

A photograph of our fabricated TLM is shown in Fig. 1b. A broadband input signal is injected from one of the ports, and it travels along the meandered microstrip line, loaded by an array of 30 switches connected in series to an array of subwavelength-spaced capacitors (unit-cell length, ~20.1 cm; Supplementary Sections 1 and 2 provide details on the TLM design and implementation). The meandered microstrip emulates an unbounded medium with close-to-linear dispersion; although the signal is fully within the TLM, a control signal for the switches is sent via a pair of much shorter microstrips (with 80 times faster transit time across the TLM), synchronously triggering all the switches with a rise time of ~3 ns, much faster than the temporal dynamics of the incoming wave (Supplementary Section 8 shows the details on switch synchronization). This switching event is much faster than half of a wave period, and its amplitude is of the order of unity, as required for efficient TR[27], resulting in an efficient time interface.

At a spatial interface (Fig. 1c), translational symmetry is broken and hence the reflected waves undergo parity inversion ($z\rightarrow -z$) and a receiver at the source location registers the features of a reflected signal in the same order as they were originally sent, akin to a sound echo. Frequency is conserved in this scenario, whereas wavevector and momentum are not. Conversely, at a time interface (Fig. 1d), time-translation symmetry is broken whereas spatial symmetry is preserved. Hence, the 'echo' associated with the time-reversed ($t\rightarrow -t$) signal is detected backwards, whereas the signal retains its original spatial profile due to momentum conservation. In addition, the broadband frequency content of the input signal is abruptly transformed, as predicted by the band diagrams of our TLM (Fig. 1e); here the blue and red lines depict the TLM dispersion curve before and after the switching, comparing the simulated (lines) and measured (circles) results. Given the small spacing between neighbouring loads compared with the relevant wavelengths, the curves follow a linear dispersion, with different slopes corresponding to the different effective capacitance before and after switching. Wave scattering at a spatial discontinuity (Fig. 1c) is equivalent to a horizontal transition in the dispersion diagram (Fig. 1e, purple arrow), preserving frequency and generating waves with new positive and negative momenta. Conversely, a time interface (Fig. 1d) corresponds to a vertical transition (Fig. 1e, green arrow), which preserves the wavenumber and generates new positive and negative frequencies, efficiently translating the entire frequency spectrum of a broadband input wave, and conserving the entire spatial structure of the pulse.

These features are clearly observed in our time-domain experimental measurements (Fig. 1f): we excite the TLM with an input signal consisting of an asymmetric pair of Gaussian pulses, measured by the input port voltage $V_1(t)$ as a first smaller pulse (yellow marker) followed by a larger one (purple marker). Approximately 15 ns after the activation of the switches (Fig. 1f (middle); Methods provides the timing details), we record the TR signal at the input port, whose zoomed-in view reveals it to be the TR copy (purple→yellow) of the input. This TR signal has inverted polarity with respect to the input signal, indicating that the TR coefficient is negative, as expected from the scattering coefficients for a reduction in wave impedance achieved by connecting the lumped capacitors in our TLM (Supplementary Section 5 shows the derivation):

$$R_{1\rightarrow 2}=\frac{Z_2\left(Z_2-Z_1\right)}{2Z_1^2} \tag{1}$$

where in our system, $Z_1\approx 50\ \Omega$ is the line impedance before switching and $Z_2\approx 25\ \Omega$ is the line impedance after switching. Approximately 140 ns later, an attenuated signal is received at the input port, corresponding to the time-refracted signal that has been travelling to the end of the TLM and then spatially reflected backwards at the mismatched termination. As expected, this second signal has inverted symmetry compared with the TR signal (yellow→purple). The TR signal, as well as the time-refracted signal at the output port V_2 (Fig. 1f, bottom), retain the same spatial profile as the incident signal due to the preserved spatial symmetry, but they slow down as they travel in a line with increased effective permittivity. This phenomenon underpins the broadband and efficient frequency translation process abruptly occurring at the time interface, based on which each frequency component of the input signal is transformed according to $\omega_1\rightarrow\omega_2=(Z_2/Z_1)\omega_1$ (Supplementary Section 5 shows the derivation).

In Fig. 2a, we retrieve the TR (R) and time-refraction (T) coefficients by performing a Fourier analysis on the measured output signals V_1 and V_2 (Fig. 1f and Supplementary Section 4); the retrieved amplitudes (top) and phases (bottom) of the temporal scattering coefficients as a function of the input wavevector k (lower horizontal axis) and corresponding input frequency (upper horizontal axis) agree well with our theoretical predictions assuming an instantaneous switching event (dashed lines). As expected, the time-refracted signal is in phase with the input, whereas the TR signal flips sign for all the input momenta of our broadband pulse spectrum. The slight wavevector dependence of the scattering coefficients at higher frequencies can be attributed to the finite switching speed (Supplementary Section 9 and 10 show an investigation of the switching rise time), the frequency dispersion associated with non-idealities of the circuit components, as well as the finite spacing between neighbouring switches.

Our results not only demonstrate efficient TR at a time interface but also imply the evidence of a new form of boundary conditions associated with time interfaces. Our platform enables fast and efficient impedance changes by adding and removing reactance to the TLM through switches, rather than modifying the reactance in time. Since the involved additional capacitors are static, this operation enables much faster transitions, without heavy requirements on energy, and hence addressing the challenges pointed out in another work[23]. In turn, our time-switched TLM does not necessarily conserve charge at the temporal boundary, different from the common assumption in the existing literature on time interfaces[9,10,17,28,29]. When closing the switches and connecting the capacitors, we do preserve the total charge in the TLM, which ensures continuity of displacement field **D**. In contrast, when we open the switches, we abruptly cutoff the charged capacitors from the TLM, creating a charge discontinuity as voltage is preserved. In other words, a new boundary condition needs to be introduced at this type of time interface, in which the electric field **E** and not **D** is conserved. This modified temporal boundary condition leads to new scattering coefficients (Supplementary Section 5):

$$R_{2\rightarrow 1}=\frac{Z_2-Z_1}{2Z_2} \tag{2}$$

which is different from equation (1). Indeed, our experiments confirm a close agreement between the experimentally retrieved scattering spectra (Fig. 2b) for the charge-discontinuous time interface and the predictions given by equation (2), and unveil the importance of considering the specific microscopic dynamics of a temporal interface to correctly predict its resulting temporal scattering.

To quantify the broadband nature of frequency translation at our photonic time interfaces, we carried out temporal scattering experiments with relatively narrowband input signals (bandwidth, ~30 MHz) at time interfaces featuring increasing (decreasing) impedance (Fig. 2c,d). We observe a clear redshift (blueshift) in the carrier frequency from $f_1=60.0$ MHz to $f_{2,\mathrm{r}}=34.5$ MHz and $f_{2,\mathrm{t}}=33.6$ MHz ($f_2=33.6$ MHz to $f_{1,\mathrm{r}}=49.5$ MHz and $f_{1,\mathrm{t}}=50.1$ MHz), accompanied by a shrinking (broadening) of the pulse width from $\Delta f_1=21.0$ MHz to $\Delta f_{2,\mathrm{r}}=\Delta f_{2,\mathrm{t}}=16.0$ MHz ($\Delta f_2=29.1$ MHz to $\Delta f_{1,\mathrm{r}}=48.3$ MHz and $\Delta f_{1,\mathrm{t}}=42.0$ MHz). In Fig. 2e,f, we sweep the input carrier wavenumbers k (bottom axes), or equivalently the input frequencies (top axes) for

https://doi.org/10.1038/s41567-023-01975-y

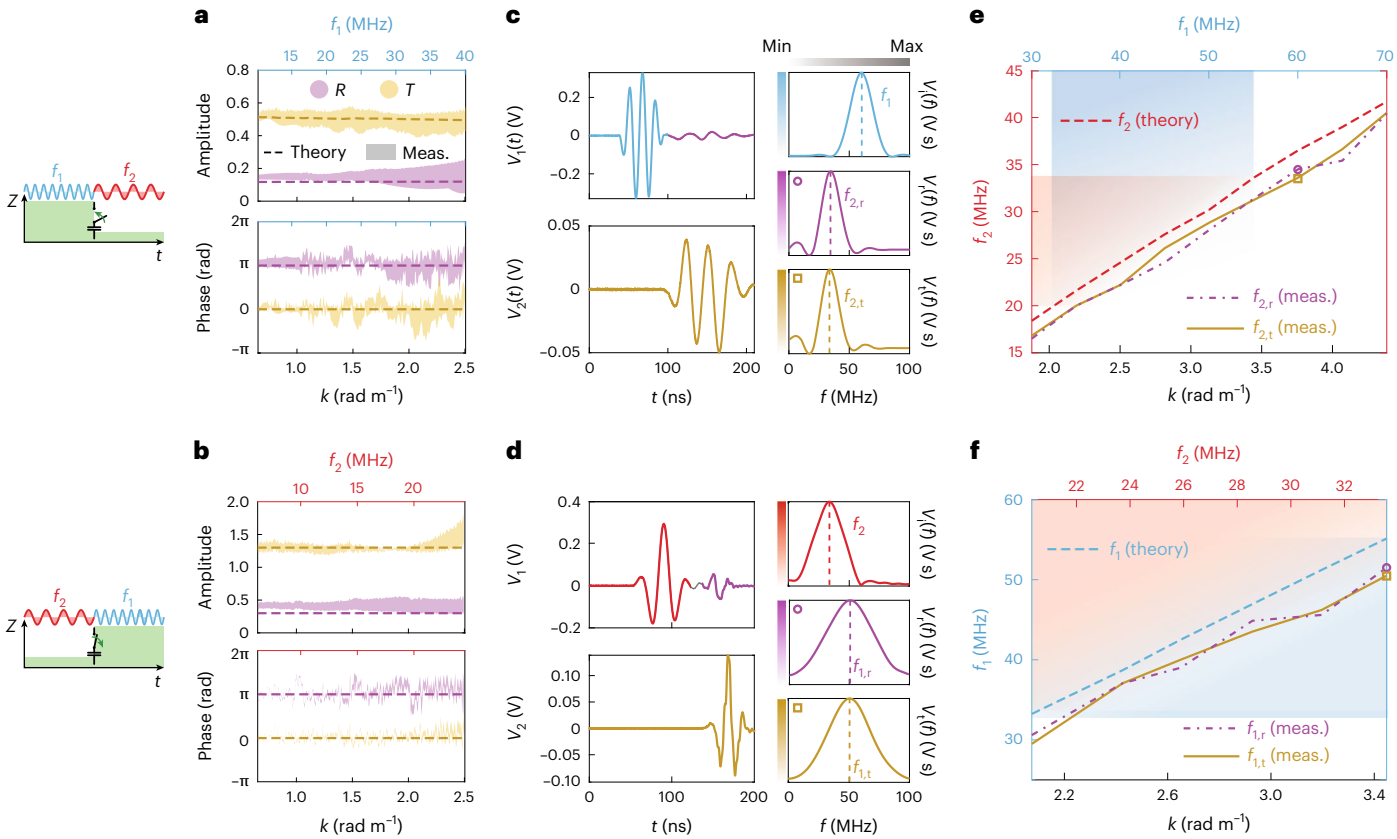

Fig. 2 | Spectral analysis of photonic TR. Schematic of the negative (top row) and positive (bottom row) switching of the effective impedance. Here f_1 (blue) and f_2 (red) denote the wave frequencies when the switches are open and close, respectively. **a**,**b**, Amplitude (top) and phase (bottom) of the spectra of the measured (shaded) and theoretical (dashed) time-refraction (T) and TR (R) coefficients on a decrease (**a**) and increase (**b**) in impedance, measured from the Fourier transforms of the respective scattered pulses. Note the π-phase shift in TR (**b**), contrasting with the TR coefficients derived in the literature when switching the medium permittivity. **c**,**d**, Carrier-wave measurements of incoming (blue), TR (purple) and time-refracted (yellow) in time (left column) and frequency (right column) domains, showing broadband redshift (**c**) and blueshift (**d**) induced by the time interface. **e**,**f**, Theoretical (dashed) and measured broadband redshift (**e**) and blueshift (**f**) of the outgoing TR (dot–dashed purple line) and time-refracted (continuous yellow line) signals induced by the time interface, obtained by scanning the carrier frequency of a narrowband input signal. The purple circles and yellow squares denote the scenarios in **c** and **d**.

the two switching scenarios, and observe the output frequency (vertical axes). When activating the time interface by closing the switches and decreasing the wave impedance (Fig. 2e), the centre frequency of both TR ($f_{2,r}$) and time-refracted ($f_{2,t}$) waves is redshifted almost uniformly by ~55%, over a range of input carrier frequencies spanning the interval of 30–70 MHz (Supplementary Section 6 shows the details on frequency translation measurements). As control experiments, we also measured the frequency upconversion by the reversed time interface (Fig. 2f). Although scanning the input frequency from 20 to 34 MHz, the observed blueshift exactly mirrors the process demonstrated in Fig. 2e. We stress that the bandwidth and linearity of the frequency conversion process at a time interface are only limited by the dispersion of our TLM, as opposed to conventional narrowband frequency conversion processes, opening exciting opportunities in a wide range of photonic applications.

By combining multiple time interfaces, it is possible to leverage TR-induced interference to more markedly manipulate the input signals. For example, by combining two time interfaces, we form a temporal slab, realized by closing and reopening the switches after a delay. These sequential TR events induce temporal wave interference. Due to causality, scattering phenomena at a temporal slab are markedly different from those in a spatial slab: although multiple scatterings occurs in a spatial slab (Fig. 3a) that generate a superposition of refracted and reflected waves, a temporal slab produces a total of four scattered waves after the second time interface (Fig. 3b). To experimentally probe the properties of the temporal slab, we launch broadband signals into our TLM (Fig. 3c, black region), and observe the total time scattering (coloured portions). For each duration of the temporal slab (τ = 15, 25 and 35 ns; Supplementary Section 7 shows the definition of τ), we indeed observe the two expected reflected pulses, each having undergone one TR and one time-refraction process, in opposite order. As opposed to conventional photonic time interfaces[9,10,29] and recent theoretical work on temporal slabs[17,28], both TR signals here are out of phase with respect to the input signal, due to the different temporal boundary condition discussed above and shown in the phase spectra in Fig. 2a,b. Importantly, all the scattered pulses have approximately the same duration as the input signal, since the second time interface converts the frequency spectrum back to the original frequencies, corresponding to two opposite vertical transitions in the dispersion diagram.

As evident in Fig. 3c, the time delay between the consecutive scattered pulses is proportional to the slab duration. This suggests that the temporal slab can be tuned to control the wave interference, thereby realizing the temporal analogue of a Fabry–Pérot etalon that enables the accurate shaping of the output frequency content. To explicitly demonstrate this effect (Supplementary Section 7), we take the Fourier transform of the TR signal $V_r(t)$, and normalize it against the transform of the input signal $V_i(t)$. This reveals the total reflection spectra (Fig. 3d) of the different temporal slabs as functions of input wavenumber k (bottom horizontal axis), or equivalently, the input frequency f_1

https://doi.org/10.1038/s41567-023-01975-y

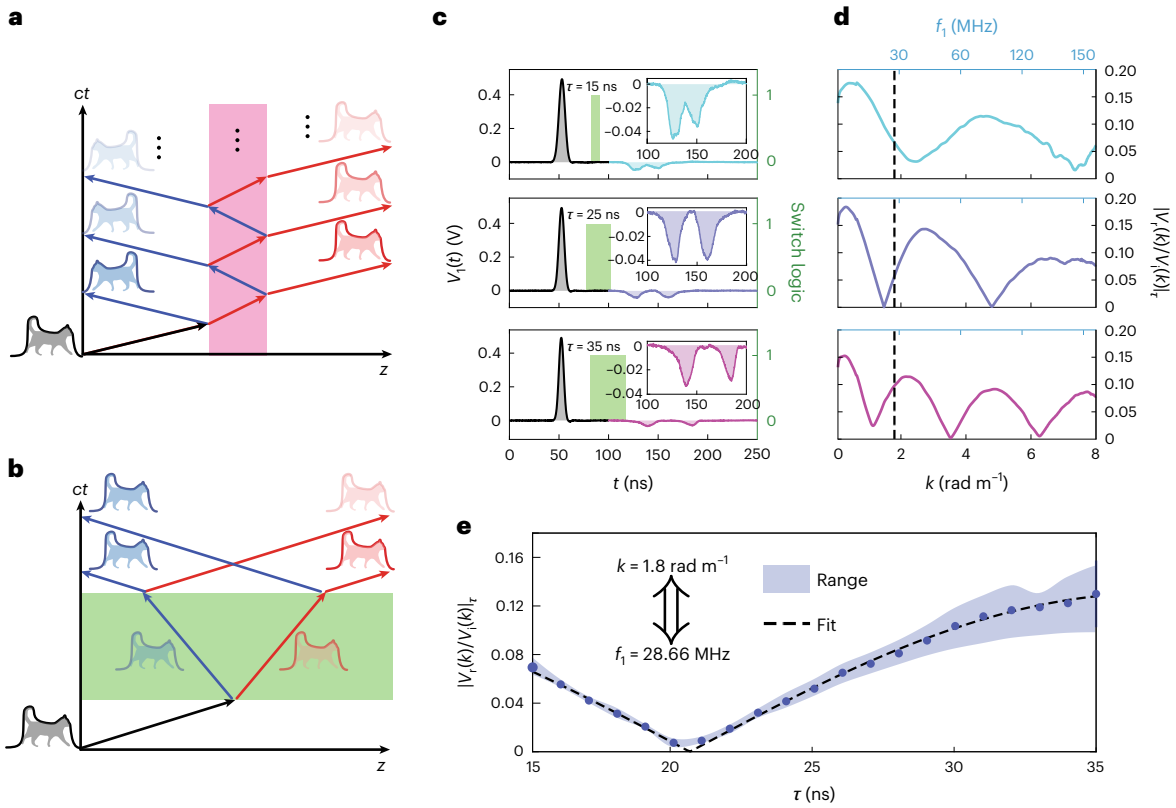

Fig. 3 | Wave scattering from a temporal slab. a,**b**, Conceptual sketches of a spatial (**a**) and temporal (**b**) slab with stepped wave impedance. Inside a spatial slab, multiple partial reflections occur, gradually decaying with increasing scattering orders, whereas in a temporal slab, only four scattered waves interfere with each other. **c**, Experimentally measured voltages at the input (V_1) and output (V_2) ports after temporal slabs with varying durations. Here $\tau \in [15, 25, 35]$ ns is the 'ON' time of the control signal, and the corresponding logic states for the switches are indicated by the green blocks. In each plot, the double reflection induced by the slab (cyan, purple and magenta portions) is clearly visible. The elapsed time between the reflected pulses is proportional to the slab duration. **d**, Normalized amplitudes of the total TR signals as a function of wavenumber k for the different temporal slabs in **c**, exhibiting zero reflection at the selected frequencies, controlled by the slab duration. **e**, For fixed k (dashed vertical line in **d**), we measure the normalized reflection amplitude as a function of switching duration τ, demonstrating large, continuous spectral tunability. The blue dots represent the average value obtained from five separate measurements, whereas the range (shaded region) shows the maximum and minimum values among the measurements.

(top axis). For each slab duration, specific values of k feature zero reflection, due to the destructive temporal interference between two TR waves, in analogy with the reflection zeroes of a Fabry–Pérot cavity. In this case, however, the associated phase accumulation does not occur in space, but rather in time. To further highlight the versatile spectral control offered by our temporal slab through temporal interference (Fig. 3e), we examine the total TR at a fixed input wavenumber of $k = 1.8$ rad m^{-1} (Fig. 3d, dashed vertical line), as we increase the slab duration, for six pulses of different half-maximum durations ranging from 5 to 10 ns, comparing the measured and theoretical results. We observe how the total amplitude of the time-reversed waves can be continuously tuned by varying τ, granting us dynamic control over wave interference at the two time interfaces without having to change the lumped capacitance values. In Supplementary Section 11, we also consider the case of an inverse slab, where the switches are first opened and then closed again.

To conclude, in this work we have reported the observation of photonic TR for broadband and efficient phase conjugation and frequency translation at single and double time interfaces, as well as the demonstration of controlled time-reversal-induced interference phenomena from a temporal slab formed by a pair of time interfaces. These results establish the key building blocks towards the realization of time metamaterials and photonic time crystals, opening a wide range of opportunities in the rising field of time-varying photonic media[26,29,30], with applications in ultrafast wave routing[19] and focusing[15,22], negative refraction[31,32], efficient and broadband spectral filtering and frequency manipulation[33], novel forms of ultrafast energy mixing[34,35], and photonic Floquet matter[4,24]. Our approach to realize time interfaces using external reactive elements added and removed through switches is key to these demonstrations, and it can be straightforwardly configured to simultaneously introduce spatial and temporal interfaces, for instance, by activating only a portion of the switches, thus blending together spatial and temporal degrees of freedom and enabling even more flexibility in wave control and manipulation. Field-programmable gate arrays controlling the switches may realize real-time reconfigurability and even self-adaptation of the response.

More broadly, our results open a pathway to employ time interfaces for broadband, efficient phase conjugation and frequency conversion arising over very short timescales, which is of great relevance for a variety of applications in electromagnetics and photonics. Efficient time reversal is important in the context of wireless communications and radar technologies, for instance, channel estimation, which is now performed through complex digital computations, to estimate complex propagation channels and compensate for signal distortion and dispersion. Broadband efficient frequency conversion is also key for applications spanning from night-vision systems to quantum photonics. Of particular interest would be to extend these concepts to higher frequencies, and we envision several available routes—from modern complementary metal–oxide–semiconductor technology (which may deliver switching speeds up to two orders of magnitude

faster than those reported here, extending the frequency range to the terahertz regime) to all-optical approaches leveraging giant nonlinearities in graphene (which offer low switching power and times as short as 260 fs (ref. [36])) or flash ionization in plasmas with even shorter switching times[37].

Online content

Any methods, additional references, Nature Portfolio reporting summaries, source data, extended data, supplementary information, acknowledgements, peer review information; details of author contributions and competing interests; and statements of data and code availability are available at https://doi.org/10.1038/s41567-023-01975-y.

References

1. Lustig, E., Segev, M. & Sharabi, Y. Topological aspects of photonic time crystals. *Optica* **5**, 1390–1395 (2018).
2. Lyubarov, M. et al. Amplified emission and lasing in photonic time crystals. *Science* **377**, 425–428 (2022).
3. Winn, J. N., Fan, S., Joannopoulos, J. D. & Ippen, E. P. Interband transitions in photonic crystals. *Phys. Rev. B* **59**, 1551–1554 (1999).
4. Dutt, A. et al. A single photonic cavity with two independent physical synthetic dimensions. *Science* **367**, 59–64 (2020).
5. Fleury, R., Khanikaev, A. B. & Alù, A. Floquet topological insulators for sound. *Nat. Commun.* **7**, 11744 (2016).
6. Cartella, A., Nova, T. F., Fechner, M., Merlin, R. & Cavalleri, A. Parametric amplification of optical phonons. *Proc. Natl Acad. Sci. USA* **115**, 12148–12151 (2018).
7. Shan, J.-Y. et al. Giant modulation of optical nonlinearity by Floquet engineering. *Nature* **600**, 235–239 (2021).
8. Hayran, Z., Chen, A. & Monticone, F. Spectral causality and the scattering of waves. *Optica* **8**, 1040–1049 (2021).
9. Morgenthaler, R. Velocity modulation of electromagnetic waves. *IRE Trans. Microw. Theory Tech.* **6**, 167–172 (1958).
10. Fante, R. L. Transmission of electromagnetic waves into time-varying media. *IEEE Trans. Antennas Propag.* **19**, 417–424 (1971).
11. Lerosey, G. et al. Time reversal of electromagnetic waves. *Phys. Rev. Lett.* **92**, 193904 (2004).
12. Fink, M. & Prada, C. Acoustic time-reversal mirrors. *Inverse Probl.* **17**, R1–R38 (2001).
13. Chumak, A. V. et al. All-linear time reversal by a dynamic artificial crystal. *Nat. Commun.* **1**, 141 (2010).
14. Vezzoli, S. et al. Optical time reversal from time-dependent epsilon-near-zero media. *Phys. Rev. Lett.* **120**, 43902 (2018).
15. Lerosey, G., De Rosny, J., Tourin, A. & Fink, M. Focusing beyond the diffraction limit with far-field time reversal. *Science* **315**, 1120–1122 (2007).
16. Mosk, A. P., Lagendijk, A., Lerosey, G. & Fink, M. Controlling waves in space and time for imaging and focusing in complex media. *Nat. Photon.* **6**, 283–292 (2012).
17. Pacheco-Peña, V. & Engheta, N. Antireflection temporal coatings. *Optica* **7**, 323–331 (2020).
18. Akbarzadeh, A., Chamanara, N. & Caloz, C. Inverse prism based on temporal discontinuity and spatial dispersion. *Opt. Lett.* **43**, 3297–3300 (2018).
19. Pacheco-Peña, V. & Engheta, N. Temporal aiming. *Light Sci. Appl.* **9**, 129 (2020).
20. Rizza, C., Castaldi, G. & Galdi, V. Short-pulsed metamaterials. *Phys. Rev. Lett.* **128**, 257402 (2022).
21. Vázquez-Lozano, J. E. & Liberal, I. Shaping the quantum vacuum with anisotropic temporal boundaries. *Nanophotonics* (2022).
22. Bacot, V., Labousse, M., Eddi, A., Fink, M. & Fort, E. Time reversal and holography with spacetime transformations. *Nat. Phys.* **12**, 972–977 (2016).
23. Hayran, Z., Khurgin, J. B. & Monticone, F. $\hbar\omega$ versus $\hbar k$: dispersion and energy constraints on time-varying photonic materials and time crystals. *Opt. Mater. Express* **12**, 3904–3917 (2022).
24. Yin, S., Galiffi, E. & Alù, A. Floquet metamaterials. *eLight* **2**, 8 (2022).
25. Engheta, N. Metamaterials with high degrees of freedom: space, time, and more. *Nanophotonics* **10**, 639–642 (2021).
26. Galiffi, E. et al. Photonics of time-varying media. *Adv. Photonics* **4**, 014002 (2022).
27. Galiffi, E., Yin, S. & Alú, A. Tapered photonic switching. *Nanophotonics* **11**, 3575–3581 (2022).
28. Mendonça, J. T., Martins, A. M. & Guerreiro, A. Temporal beam splitter and temporal interference. *Phys. Rev. A* **68**, 043801 (2003).
29. Caloz, C. & Deck-Leger, Z.-L. Spacetime metamaterials—part II: theory and applications. *IEEE Trans. Antennas Propag.* **68**, 1583–1598 (2020).
30. Caloz, C. & Deck-Leger, Z.-L. Spacetime metamaterials—part I: general concepts. *IEEE Trans. Antennas Propag.* **68**, 1569–1582 (2020).
31. Pendry, J. B. Time reversal and negative refraction. *Science* **322**, 71–73 (2008).
32. Bruno, V. et al. Negative refraction in time-varying strongly coupled plasmonic-antenna–epsilon-near-zero systems. *Phys. Rev. Lett.* **124**, 43902 (2020).
33. Miyamaru, F. et al. Ultrafast frequency-shift dynamics at temporal boundary induced by structural-dispersion switching of waveguides. *Phys. Rev. Lett.* **127**, 053902 (2021).
34. Li, H., Yin, S., Galiffi, E. & Alù, A. Temporal parity-time symmetry for extreme energy transformations. *Phys. Rev. Lett.* **127**, 153903 (2021).
35. Carminati, R., Chen, H., Pierrat, R. & Shapiro, B. Universal statistics of waves in a random time-varying medium. *Phys. Rev. Lett.* **127**, 94101 (2021).
36. Ono, M. et al. Ultrafast and energy-efficient all-optical switching with graphene-loaded deep-subwavelength plasmonic waveguides. *Nat. Photon.* **14**, 37–43 (2020).
37. Nishida, A. et al. Experimental observation of frequency up-conversion by flash ionization. *Appl. Phys. Lett.* **101**, 161118 (2012).

Methods

Simulations

All the circuit simulations are performed in Keysight Advanced Design Systems. Time-domain simulations are carried out using the Transient Solver, whereas frequency-domain analysis is done with the S-Parameter Solver.

The main TLM carrying the signal is modelled with physical transmission-line sections with characteristic impedance $Z_0 = 50\ \Omega$, length $d = 0.208$ m, effective dielectric constant $\varepsilon_{r,eff} = 8.36$, attenuation constant $\alpha = 0.5$ (at $f = 100$ MHz) and dielectric loss tangent $\tan\delta = 0.0019$. It should be noted that the effective dielectric constant of 8.36 is consistent with expectations from well-known design formulas with microstrip lines. To further model the non-idealities associated with our manufactured circuit, each unit cell is connected to its nearest neighbour with a 2 pF capacitor, and to its second-nearest neighbour with a 1 pF capacitor. This models the parasitic capacitive coupling between the unit cells, which limits our operating bandwidth by introducing dispersion and bandgaps. These values are found to produce consistently good matches between the experimental and simulation results.

The switches are implemented as ideal voltage-controlled reflective switches with 1 Ω resistance in the ON state. Each switch connects a node on the transmission line to a series *RLC* circuit, with an 82 pF capacitor representing the load, a 4 Ω resistor representing the parasitic losses and an 8 nH inductor representing the parasitic inductance of the grounding vias. These values are extracted from the measurements of a single unit cell: the parasitic component values are swept in frequency-domain simulations until a good match with the measured S-parameters is observed.

Experiments

The TLM sample is fabricated in-house using a 1.52-mm-thick Rogers TMM 13i substrate, which has a nominal dielectric constant of 12.85 ± 0.35, and a loss tangent of 0.0019. Supplementary Sections 1 and 2 show the details of the circuit layout and choices of all the circuit components.

During our measurements, the input signal consists of a train of repeated copies of an arbitrarily shaped pulse. Since the input pulses generally have durations in the order of tens of nanoseconds, which is much shorter than the period of the pulse train (>1 μs), we can effectively treat each pulse as a single isolated event. The signals entering the TLM through the input port is probed with a T-connector attached to an oscilloscope, whereas the exiting signals are directly probed with the scope. Supplementary Section 2 shows a simplified schematic of the experimental setup.

To control the switches, we use a rectangular pulse train that is phased locked to the input pulse train. By adjusting the relative phase between the two signals, we can control the timing of the interface. The switches that we used have internal grounding circuitry which, on opening, will dissipate all the charges stored on the capacitor. This is crucial for accurately realizing our two distinct types of time interface.

To induce temporal reflection, we activate the switches after the input signal is registered in $V_{o1}(t)$, but before it is recorded in $V_{o2}(t)$, corresponding to a time when the signal is completely contained within the TLM. The TR signal will travel backwards towards port 1 of the transmission line, where it will again enter the input T-connector. Identical copies of the TR (with 3.5 dB attenuation) are fed to the source and oscilloscope. Hence, the actual amplitude of the temporal reflection generated by our time interface is larger than that recorded by port 1. Supplementary Information details the effect of the T-connector and impedance mismatch.

To measure the frequency translation of our time interface, we launched signals with varying carrier frequencies into the transmission line, and observed the TR as well as refracted signals. Supplementary Sections 6 and 12 provide a typical time-domain measurement result, and the accounting of video leakage. We performed a Fourier analysis on the time-gated incident, refracted and reflected signals to observe their individual frequency content. The frequency spectra for each signal will consist of a sharp peak, aligned with its centre frequency.

Data availability

All data that support the plots within this paper and other findings of this study are available from the corresponding author upon reasonable request. Source data are provided with this paper.

Code availability

The codes that support the findings of this study are available from the corresponding author upon reasonable request.

Acknowledgements

This work was supported by the Air Force Office of Scientific Research MURI program with grant no. FA9550-18-1-0379, the Simons Collaboration on Extreme Wave Phenomena and a Vannevar Bush Faculty Fellowship. A.A. acknowledges support from the Army/ARL via the Collaborative for Hierarchical Agile and Responsive Materials (CHARM) under cooperative agreement W911NF-19-2-0119. E.G. was supported by the Simons Foundation through a Junior Fellowship of the Simons Society of Fellows (855344).

Author contributions

H.M. and G.X. designed the TLM circuit and carried out the circuit simulations and measurements. S.Y. developed the theory, with contribution from E.G. and A.A. G.X. and S.Y. interpreted and presented the experimental data, with contribution from E.G. H.M., G.X. and S.Y. wrote the material for the Supplementary Information. E.G. led the writing of the paper, with contribution from all the authors. Y.R. and G.X. fabricated the TLM. A.A. conceived the problem and supervised the project.

Competing interests

The authors declare no competing interests.

Additional information

Extended data is available for this paper at https://doi.org/10.1038/s41567-023-01975-y.

Supplementary information The online version contains supplementary material available at https://doi.org/10.1038/s41567-023-01975-y.

Correspondence and requests for materials should be addressed to Andrea Alù.

Peer review information *Nature Physics* thanks Ching Hua Lee and the other, anonymous, reviewer(s) for their contribution to the peer review of this work.

https://doi.org/10.1038/s41567-023-01975-y

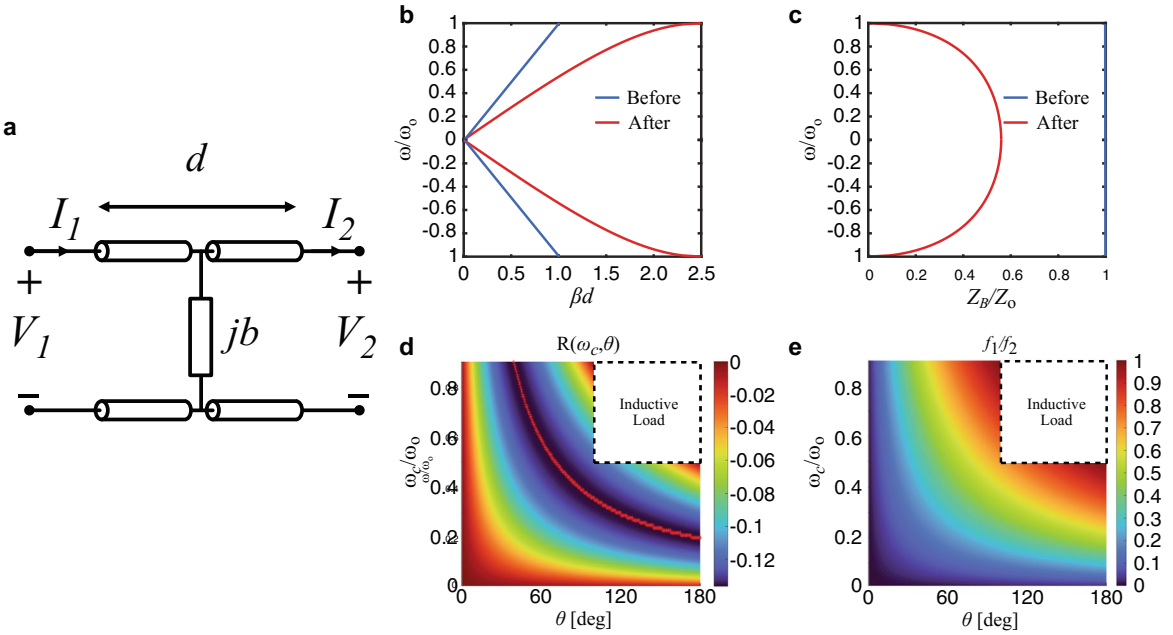

Extended Data Fig. 1 | Design and analysis of the TLM. (**a**) Equivalent T-network for one unit cell of our TLM when the switches are closed. Here, d is the physical length of the unit cell (0.2080 m) and $jb=j2.753$ is the normalized load susceptance at 100 MHz. (**b**) Normalized dispersion relation and (**c**) normalized Bloch impedance of our transmission line, assuming a unit-cell electrical length of $\theta=kd=72°$, and an normalized load susceptance of $b=2.753$, both evaluated at 100 MHz. The blue lines and the red lines correspond to the unloaded and the loaded lines respectively. In order to identify the optimal unit-cell electrical length θ and cutoff frequency of the first band gap ω_c, which is related to the load susceptance b, two dimensional parametric studies were done to generate maps of (**d**) the temporal reflection coefficient and (**e**) the frequency translation ratio. The red line in panel (a) corresponds to the combination of (θ,ω_c) that yields the largest reflection coefficient. The white boxes with dotted borders in both panels denote regions in which the load susceptance become inductive (that is, negative).

https://doi.org/10.1038/s41567-023-01975-y

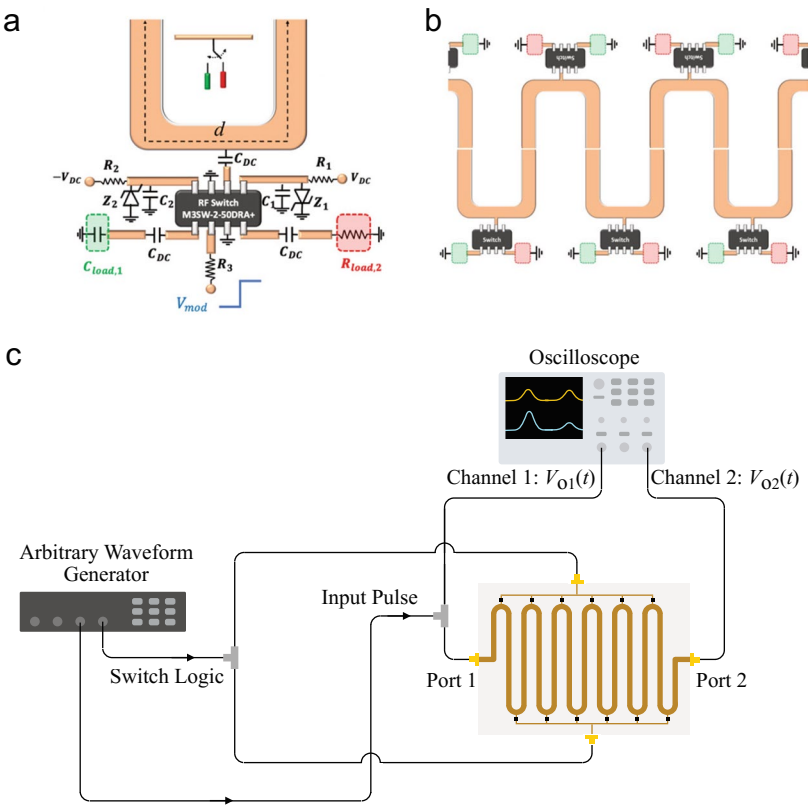

Extended Data Fig. 2 | Practical circuit layout and measurement setup. (**a**) Layout for the unit cell. The descriptions of the components can be found in Supplementary Table 1. (**b**) Schematic for the complete TLM, showing how the unit cells are connected. (**c**) Simplified schematic of the experimental set up for time domain measurements. Power supply for the switches and a separate function generator for switch control are not shown.

https://doi.org/10.1038/s41567-023-01975-y

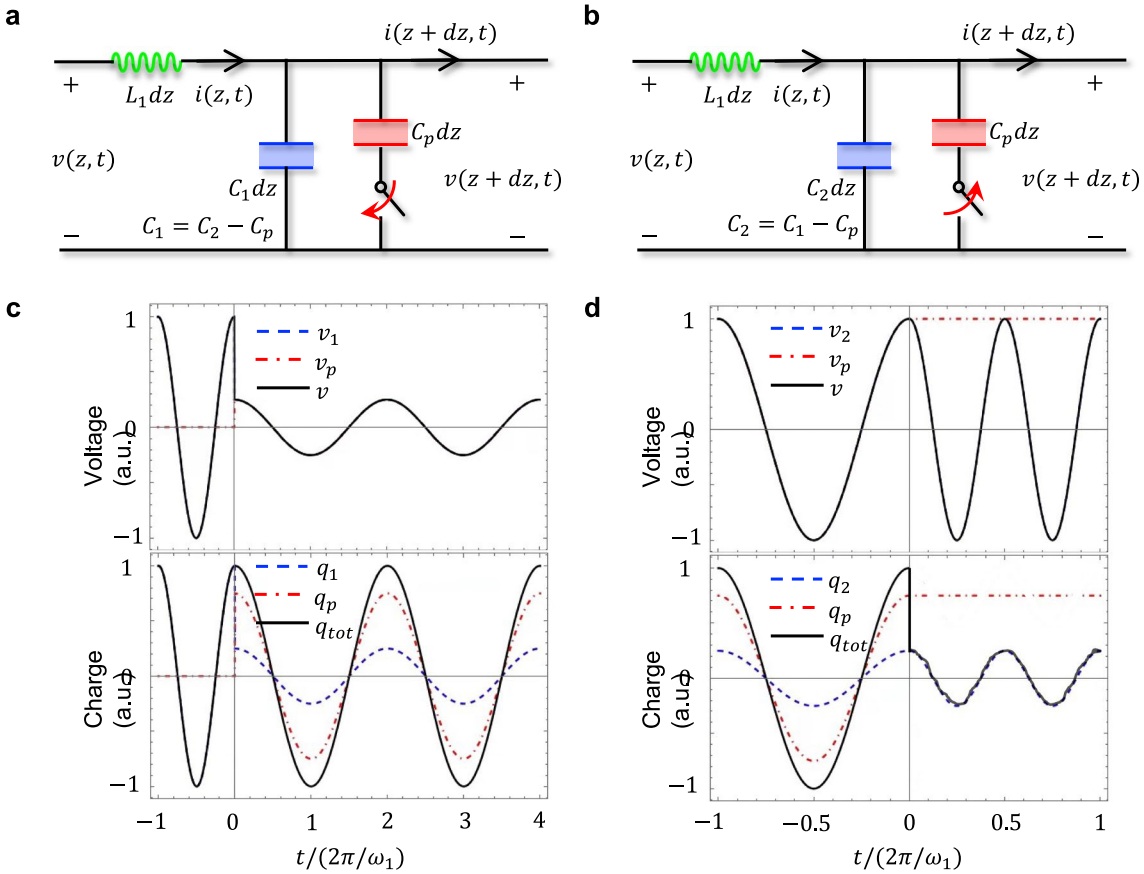

Extended Data Fig. 3 | Circuit model of time-switched transmission-line (TL). Panels (**a**) and (**b**) correspond to the loading and removal of a shunt capacitor respectively. C_1(C_2) denotes the value of effective distributed capacitance of the TL before (after) closing or opening the switch. Panel (**c**) demonstrates the time variation of voltages and charges on each capacitor, as well as their total values sensed by the TL, corresponding to a numerical example of panel (a) with C_2=4C_1. Panel (**d**) shows the same quantities for a numerical example of Panel B with C_2=C_1/4.

https://doi.org/10.1038/s41567-023-01975-y

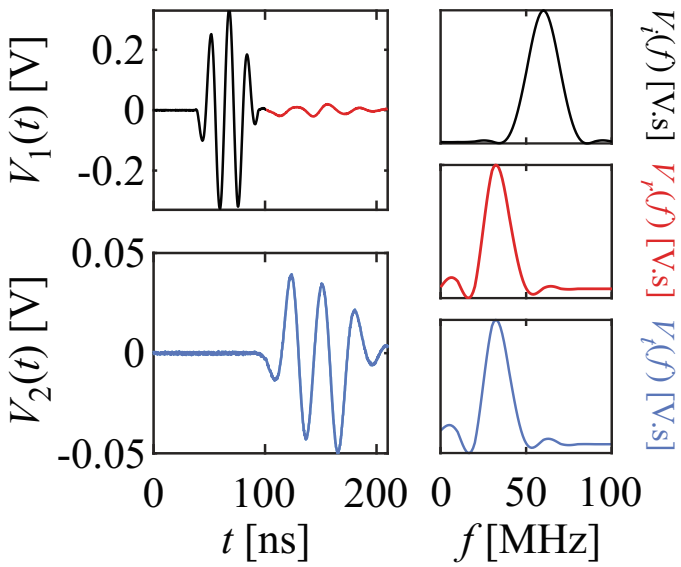

Extended Data Fig. 4 | A sample of the measurement used to characterize the frequency conversion of our time-interface when the wave impedance reduced. The left column shows the incident (black), time-reflected (red) and time-refracted (blue) signals. The right column shows their corresponding Fourier transform. A frequency down conversion by about 0.55 is clearly visible through the peak of the frequency spectra.

https://doi.org/10.1038/s41567-023-01975-y

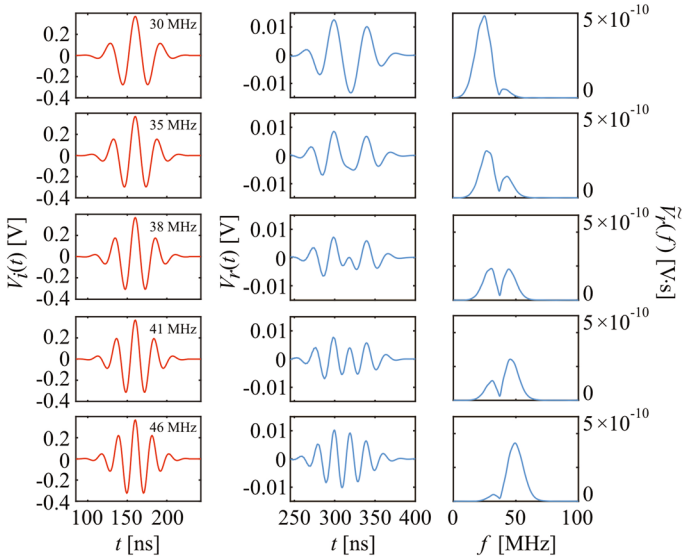

Extended Data Fig. 5 | Circuit simulations for a temporal slab with a fixed 'ON' time (τ = 15 ns). The injected pulses are in the form of Gaussian wave packets with different carrier frequencies and 17.5 MHz spectral FWHM. The simulated circuit consists of 3 cascaded copies of our TLM sample. The left column depicts the time domain waveform of the input pulse, while the middle column shows the total time-reflected output. The right column shows the frequency spectra of the output. All of the spectra exhibit reflection nulls at approximately 38 MHz, which agrees with measured results in Fig. 3d of the main text.

https://doi.org/10.1038/s41567-023-01975-y

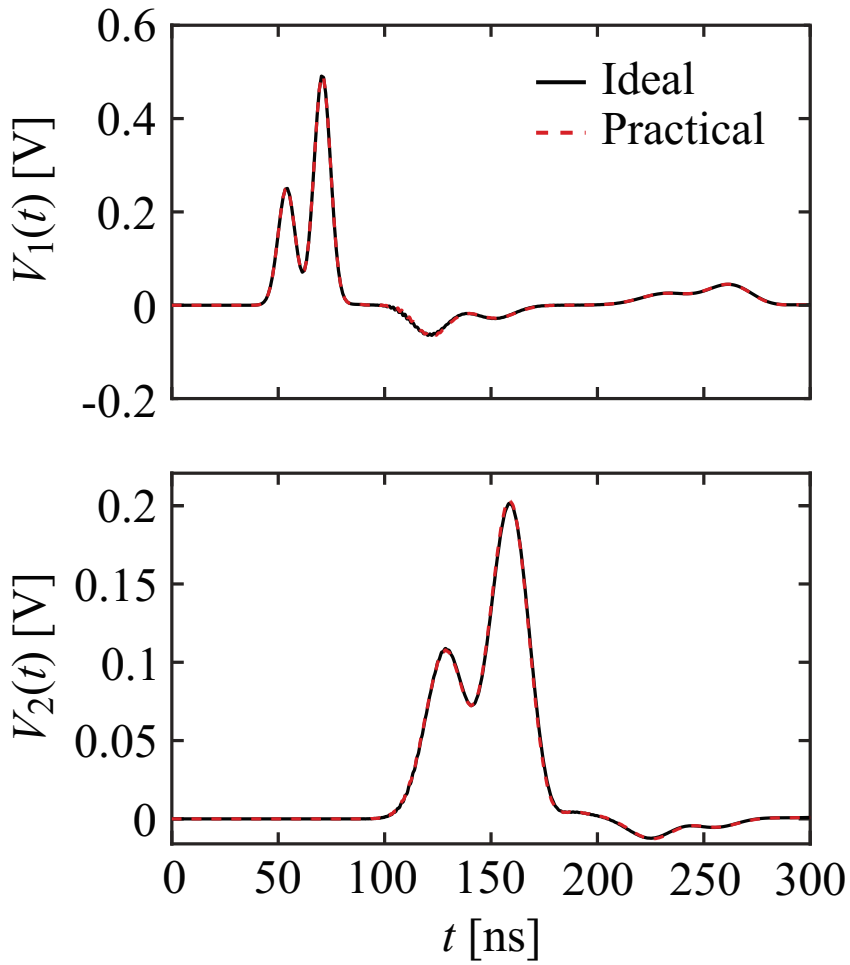

Extended Data Fig. 6 | Circuit simulations demonstrating the effect of switch desynchronization. The black curve corresponds to the simulated voltages at ports 1 and 2 assuming perfect synchronization. The red curve ('Practical'), which matches the ideal one almost exactly, depicts the simulation of our measurement set up. This shows that despite the finite time delay between adjacent unit cells, our set up can emulate a homogeneous time-interface with very high fidelity.

https://doi.org/10.1038/s41567-023-01975-y

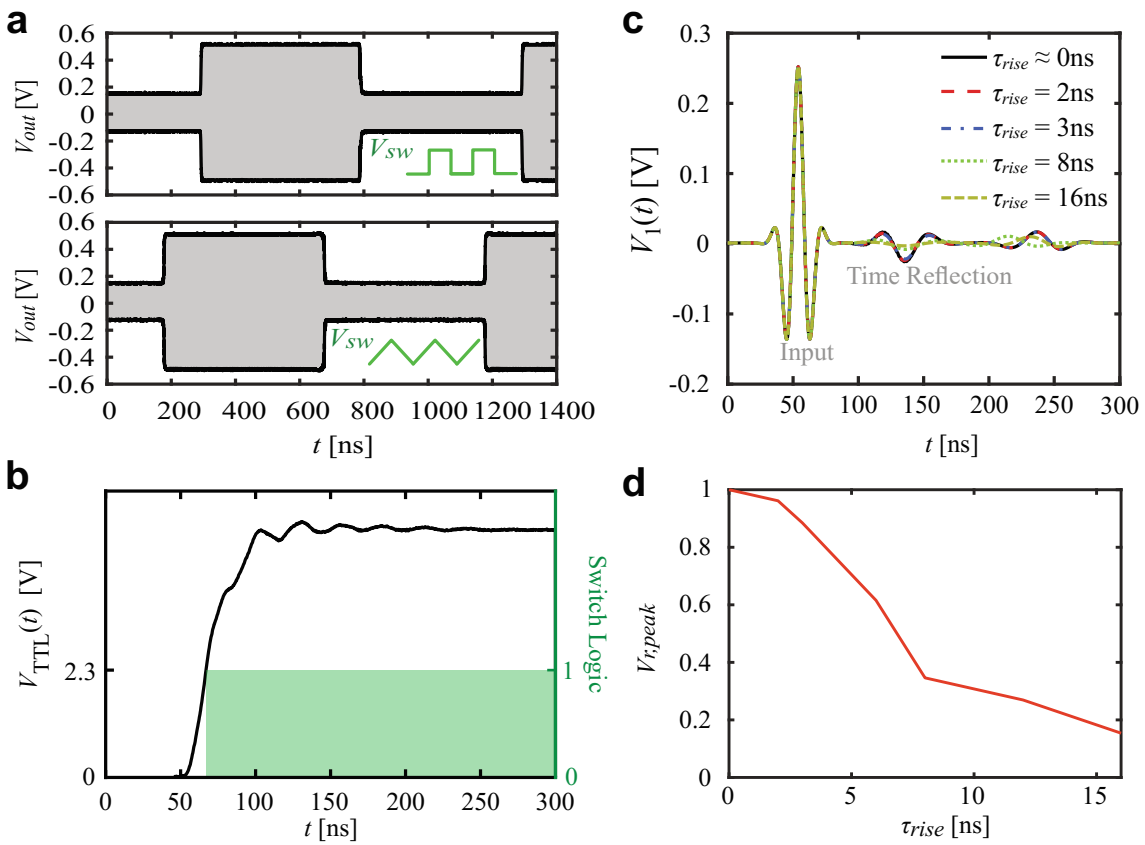

Extended Data Fig. 7 | Investigation on the effect of finite switching time. (**a**) Experimental characterization of the circuit switching speed using different types of control signal. Here, a 100 MHz sinusoidal signal is transmitted through a single unit cell sample of the TLM, and the envelope of the output waveform is recorded (black curve). We activate the switch inside the unit cell using different types of control signals V_{sw}, with drastically different slopes. Both a rectangular control signal (top) and a triangular control signal (bottom) produced identical output envelopes, demonstrating that the rise time of V_{sw} has very little influence on the switching speed of the circuit. (**b**) A sample measurement of the control signal used to induce the time-interface. The slew rate of the signal is very low, due to the input reactance of the switches. However as shown in panel (a), simply crossing the activation threshold of the switch (2.3 V according to the datasheet) is sufficient to induce a sharp time-interface. This particular control signal was used to induce the time-interface examined in Fig. 2e of the main text. To further verify the fidelity of the time interface, we perform circuit simulation of the TLM with different 10%-to-90% rise time for the switches, and plot the (**c**) time domain voltage measured at the input port. The input is a Gaussian wave packet with 50 MHz center frequency and 40 MHz spectral FWHM. The blue curve represents the simulation results when the circuit has the same rise time (3 ns) as our selected RF switches; it is seen to closely match the black curve, which corresponds to the case when the rise time is near zero. As we further increase the rise time to 8 ns (green) and 12 ns (yellow), the amplitude of the time reflection become significantly weaker. (**d**) Peak amplitude (normalized against the ideal case) of the time reflected wave packet as a function of the switch rise time. The amplitude corresponding to the case of 3 ns rise time was approximately 90% of the ideal amplitude.

https://doi.org/10.1038/s41567-023-01975-y

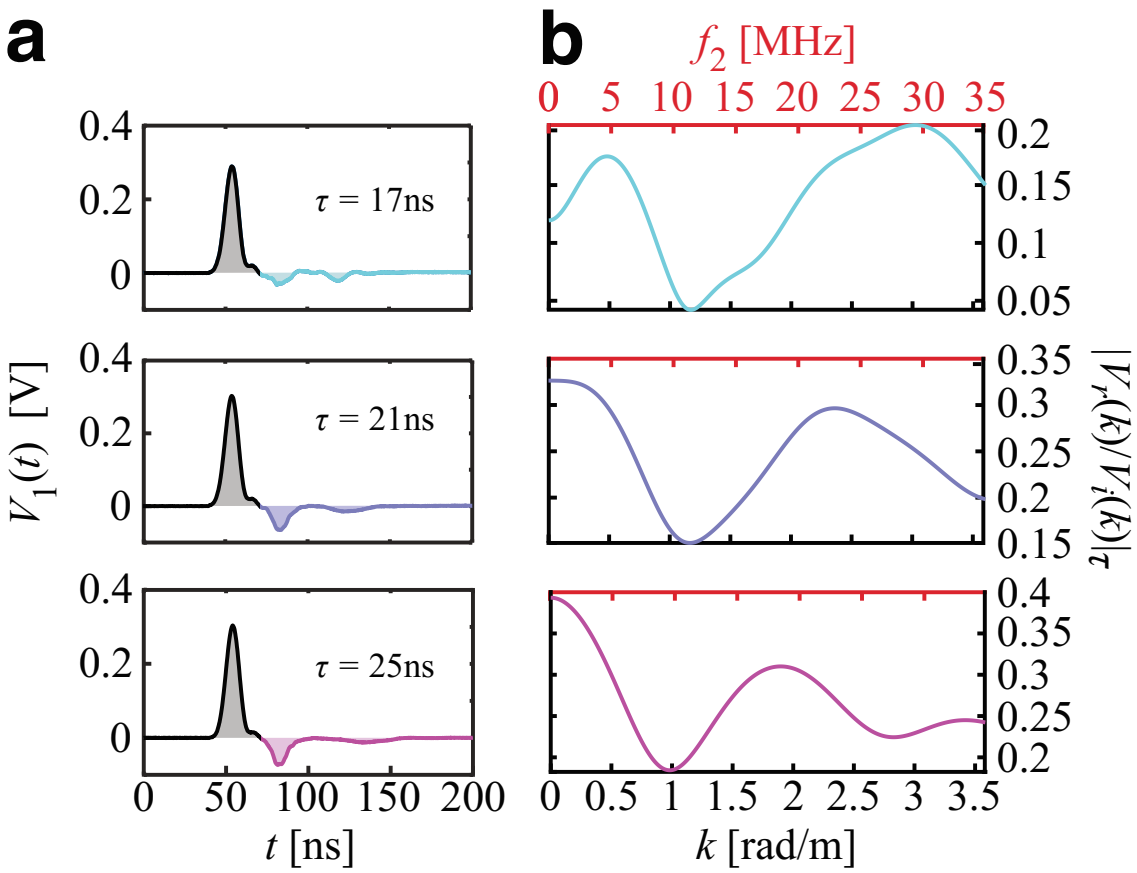

Extended Data Fig. 8 | Measurement of temporal interference induced by the inverted temporal slab. (**a**) Time domain waveform recorded at port 1 for various values of 'OFF' duration τ. As τ is increased, so does the separation between the two TR pulses. The second TR pulse is heavily attenuated for larger values of τ, since it experiences increased attenuation. (**b**) Reflection spectra of inverted temporal slab in the wavenumber (bottom axis) and frequency (top axis) domain. We see distinct reflection minima whose locations are tunable via adjustment of τ.

https://doi.org/10.1038/s41567-023-01975-y

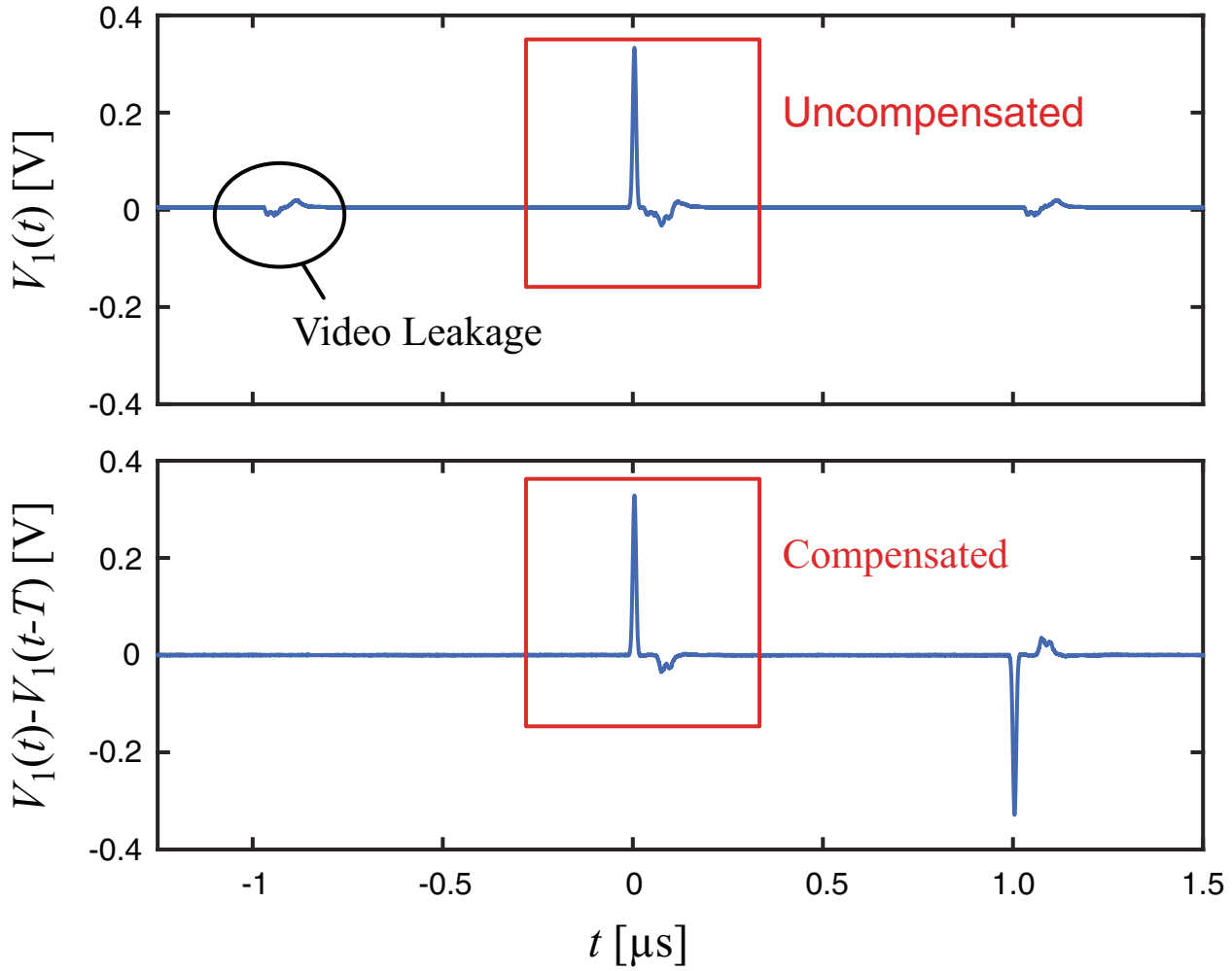

Extended Data Fig. 9 | Compensation of video leakage from the switches. Top plot shows the uncompensated waveform measured at the input port of the TL, with multiple spurious spikes caused by the rising and falling edges of our control signal. The bottom plot shows the compensated waveform, obtained through subtracting the top plot by a shifted copy of itself. The compensated waveform has much more clearly observable input and TR pulses. A spurious inverted copy of the main signal remains, but can be discarded during analysis.

https://doi.org/10.1038/s41567-023-01975-y

Extended Data Table 1 | List of components used to fabricate our transmission line, referred to the schematic shown in Supplementary Fig. 4

Component	Description	Value	Component Number
C_{DC}	DC blocking capacitor	3.9 nF	C0402C392K5RACAUTO
$C_{1,2}$	RF shorting capacitor	10 pF	06031A100GAT2A
$R_{1,2}$	Resistor	11.5 Ohm	RK73H1JTTD11R5F
R_3	Resistor	100 Ohm	RK73H1JTTD1000F
$Z_{1,2}$	Zener Diode	V_z = 5.3V	MMSZ4690T1G
RF Switch			M3SW-2-50DRA+
$R_{load,2}$	TL load (OFF state)	1 MOhm	RCS12061M00JNEA
$C_{load,1}$	TL load (ON state)	82 pF	C0402C823K9RACTU